SCIENTIFIC REPORTS
nature research

OPEN

Morphological, optical and photovoltaic characteristics of $MoSe_2/SiO_x/Si$ heterojunctions

J. P. B. Silva[1*], C. Almeida Marques[2,3], A. S. Viana[4], L. F. Santos[5], K. Gwozdz[6], E. Popko[6], J. P. Connolly[7], K. Veltruská[8], V. Matolín[8] & O. Conde[2,3*]

This work reports the effect of different processing parameters on the structural and morphological characteristics of $MoSe_2$ layers grown by chemical vapour deposition (CVD), using MoO_3 and Se powders as solid precursors. It shows the strong dependence of the size, shape and thickness of the $MoSe_2$ layers on the processing parameters. The morphology of the samples was investigated by field emission scanning electron microscopy (FESEM) and the thickness of the deposited layers was determined by atomic force microscopy (AFM). Raman and photoluminescence (PL) spectroscopies were used to confirm the high quality of the $MoSe_2$ layers. Surface composition was examined by photoelectron spectroscopy (XPS). Moreover, the $MoSe_2/SiO_x/Si$ heterojunctions exhibit diode behaviour, with a rectification ratio of 10, measured at ± 2.0 V, which is due to the p-i-n heterojunctions formed at the p-Si/SiO_x/$MoSe_2$ interface. A photovoltaic effect was observed with a short circuit current density (J_{sc}), open circuit voltage (V_{OC}) and efficiency of -0.80 mA/cm^2, 1.55 V and 0.5%, respectively. These results provide a guide for the preparation of p-i-n heterojunctions based on few-layer $MoSe_2$ with improved photovoltaic response.

It has recently been shown that two dimensional semiconductor transition metal dichalcogenides (2D TMDs) have solved the zero-band gap drawback of graphene. They have furthermore attracted considerable attention due to their outstanding properties for various optical and photoelectrical applications[1,2]. In the past few years, Chemical Vapour Deposition (CVD) has been shown to allow the growth of large-scale monolayers of graphene[3], boron nitride[4] and TMDs[5–9] of high quality, comparable to the quality of exfoliated monolayers, which makes CVD very promising regarding the fabrication of such layers on an industrial scale. Amongst the semiconductor TMDs deposited by CVD, selenides have been received less attention. This is possibly due to the lower chemical reactivity of selenium in relation to sulfur, which implies longer reaction times for large-scale deposition, inevitably leading to thicker films[10,11]. However, compared to the sulfides, monolayer $MoSe_2$ has a direct band gap of 1.5 eV, close to the optimum band gap value needed for solar spectrum related applications, such as single-junction solar cells and photoelectrochemical cells[12]. Moreover, the larger spin-splitting energy of ~180 meV at the top of the valence band makes $MoSe_2$ an interesting material for spintronics[9,13].

Semiconductor TMDs have been deposited onto sapphire[14], mica[13] and oxidized silicon[8] substrates. Besides its importance as a dielectric layer for the fabrication of electronic and optoelectronic devices, the presence of a SiO_x interlayer between the Si substrate and the TMD layers brings other advantages. The oxide layer can be easily removed by chemical means without degrading the deposited layer, enabling its suspension and transfer to other substrates (e.g. flexible substrates) as well as the integration in low dimensional devices, as 2D building blocks[15], without the need of exfoliation methods. Furthermore, depending on the SiO_x layer thickness, it can

[1]Centro de Física das Universidades do Minho e do Porto (CF-UM-UP), Campus de Gualtar, 4710-057, Braga, Portugal. [2]Departamento de Física, Faculdade de Ciências, Universidade de Lisboa, 1749-016, Lisboa, Portugal. [3]CeFEMA-Center of Physics and Engineering of Advanced Materials, Universidade de Lisboa, 1749-016, Lisboa, Portugal. [4]Centro de Química e Bioquímica e Centro de Química Estrutural, Departamento de Química e Bioquímica, Faculdade de Ciências, Universidade de Lisboa, 1749-016, Lisboa, Portugal. [5]Centro de Química Estrutural/Departamento de Engenharia Química, Instituto Superior Técnico, Universidade de Lisboa, 1096-001, Lisboa, Portugal. [6]Department of Quantum Technologies, Wroclaw University of Science and Technology, Wroclaw, 50-370, Poland. [7]GeePs, UMR CNRS 8507, (IPVF), 11 rue Joliot Curie, Plateau de Moulon, 91192, Gif sur Yvette, France. [8]Department of Surface and Plasma Science, Faculty of Mathematics and Physics, Charles University, V Holešovičkách 2, Staré Město, 18000, Prague 8, Czech Republic. *email: josesilva@fisica.uminho.pt; omconde@ciencias.ulisboa.pt

Sample	mass (*Se*) /mass (MoO_3)	H_2 (%)	Total flow rate (sccm)
A	1.00	16.7	60
B	1.00	8.3	60
C	1.50	16.7	60
D	7.63	16.7	60
E	1.94	8.3	60

Table 1. Growth parameters used in the CVD of the $MoSe_2$ nanolayers.

produce sufficient optical contrast with respect to the deposited nanolayers, facilitating their detection by optical microscopy[16,17].

Regarding applications, $MoSe_2$ is used as an active layer in resistive random access memories (RRAMs)[18,19] and as a complement for $Cu(In,Ga)(Se,S)_2$ (CIGS) solar cells[20], as well as in homo and heterojunctions with other TMD materials[21]. However, there are no reports concerning the photovoltaic (PV) characteristics of $MoSe_2$ film in a p-i-n configuration, in spite of the fact that the integration of TMDs on Si could significantly lower the cost of photovoltaic and multifunctional devices[22].

Here, we study the PV effect of mono- to few-layered $MoSe_2$ flakes deposited by CVD onto SiO_x/p-type Si substrates (p-i-n vertical heterostructure) and discuss in detail the PV mechanism in the heterojunctions.

Results and Discussion

It is well known that mono-to-few layer $MoSe_2$ can be grown by CVD, using MoO_3 and Se as solid precursors, providing hydrogen is added to the carrier gas[2,9,10,23,24]. The role of H_2 is to reduce the MoO_3 vapour to MoO_{3-x} and enhance the reaction with Se vapour. However, the relative amount of H_2 in the total flowing gas that leads to similar layer morphology for different CVD reactors, depends on their specific characteristics, such as the temperature profile along the CVD furnace, which in turn imposes limits on the distance between the precursors' holders. Furthermore, also the mass ratio between the solid precursors is crucial for large-area monolayer growth[9,10,23] due to the low chemical reactivity of Se. This mass ratio therefore needs to be optimized.

In this work we analyse the microstructure and morphology of five samples prepared with different values of H_2% in the gas phase and of $m(Se)/m(MoO_3)$ mass ratio (Experimental section, Table 1).

Addressing first the issue of the H_2% in the gas phase, Fig. 1 shows the SEM micrographs of samples A (Fig. 1a) and B (Fig. 1b), and their corresponding AFM images (Fig. 1c,d), respectively), and height profiles taken along the white lines on each image. The formation of triangular flakes, which are characteristic of $MoSe_2$ mono- to few-layer structures, can be observed in both samples.

However, while sample A displays the presence of triangles with an average lateral size of 154 ± 27 nm and covering about 18% of the sample's surface area, sample B shows the triangles which are 247 ± 100 nm wide and which occupy ~31% of the surface area, resembling an almost continuous thin film.

The AFM image of sample A reveals triangles with round vertices, where some are 0.79 nm thick (profile 1), corresponding to the reported value for monolayer $MoSe_2$, whereas the few-layer structures (profile 2) are indeed bilayers.

The AFM image of sample B shows multilayer triangular pyramids with lateral sizes ~320 nm, as well as smaller triangles with ~185 nm edges. In this figure, one can distinguish the different layers in each pyramid. Height profile 1 shows that the smaller triangles are monolayers of thickness 0.85 ± 0.06 nm, whereas the one measured along line 2 indicates that pyramids are 5-layer $MoSe_2$ with thicknesses varying between 0.59 and 1.07 nm, showing evidence of a layer-by-layer growth process.

This H_2% study shows that 8.3% of H_2 in the total gas flux (sample B) allows the deposition of mono- to multilayer $MoSe_2$ structures, with larger lateral sizes and covering a higher surface area. However, although the better morphology suggests a higher material quality, more multilayer structures are found in sample B.

Secondly, addressing the $m(Se)/m(MoO_3)$ mass ratio, samples C, D and E were synthesized by increasing the $m(Se)/m(MoO_3)$ ratio up to ≤ 8 while using the previous values for the $\%H_2$ (Experimental section, Table 1). Figure 2 shows the SEM micrographs, AFM images and height profiles for these samples and the overall results are summarized in Table 2.

In sample C, the triangles are sparsely distributed on the surface giving rise to a non uniform surface density that is as low as 3.3 ± 0.7% in some regions of the sample, while attaining a value of 15 ± 2% in others, thus comparable with the one observed in sample A; nevertheless, they have more regular shape and larger lateral sizes. The AFM analysis of this sample reveals multilayer growth. Regarding sample E, a large amount of triangles with different lateral sizes, with an average of 278 ± 89 nm, in which the larger triangles are merged with smaller ones, can be observed. This sample displays the highest value of surface area covered by triangles. Sample E, as well as D, is dominated by the presence of mono- and bi-/trilayers $MoSe_2$ flakes with large sizes. These two samples were selected for further studies.

Raman spectroscopy was performed to assess the structural quality of the $MoSe_2$ flakes and to get a confirmation on the number of layers measured by AFM. Figure 3a shows the Raman spectra of samples D and E, respectively.

Raman spectra exhibit peaks at 161.3, 240.8, 287.3 and 352.4 cm^{-1} for sample D and 168.7, 241.4, 286.5 and 352.4 cm^{-1} for sample E. These Raman shifts correspond to the E_{1g}, A_{1g}, E^1_{2g} and B^1_{2g} modes of $MoSe_2$, respectively. In particular, the A_{1g} and E^1_{2g} modes located close to 241 and 287 cm^{-1} have been assigned to monolayer $MoSe_2$[8,13,21], along with a value of 46 ± 1 cm^{-1} for the difference $\Delta(E^1_{2g} - A_{1g})$[8,13,25]. Since the B^1_{2g} mode is absent

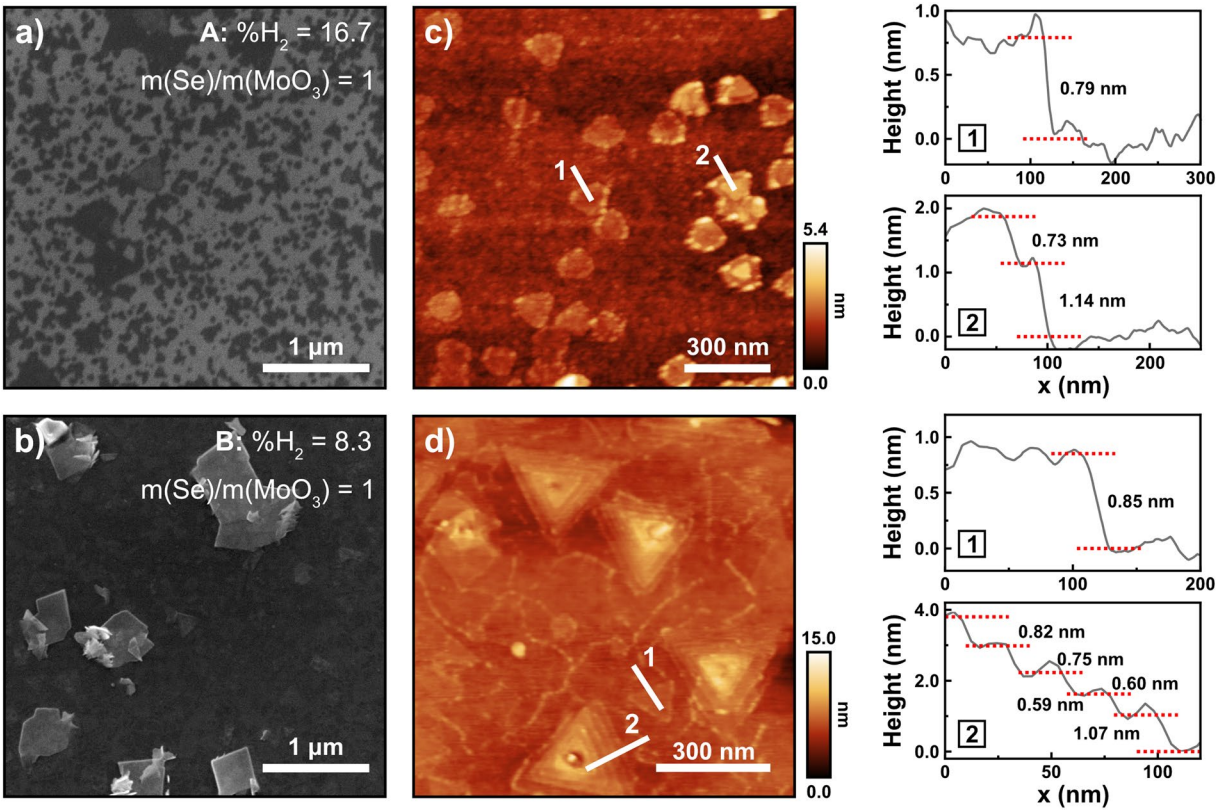

Figure 1. Scanning electron micrographs (**a**,**b**) of samples A and B, respectively, and their corresponding AFM images (**c**,**d**). The height profiles, taken along lines 1 and 2 on the AFM images, are shown on the right panel.

in the monolayers, the weak peak at 352.4 cm^{-1} reveals the presence of bi- and tri-layers[8,21], in agreement with the AFM measurements.

Figure 3b displays the photoluminescence spectra of samples D and E showing a PL peak at 794 nm (1.56 eV), which is close to the reported band gap value of $MoSe_2$ monolayer[25]. The fact that both samples show photoluminescence for the same wavelength is a consequence of their similarity in terms of number of layers. The difference in PL intensity between the two samples can be explained by the smaller lateral size of the triangles in sample D, which results in more grain boundaries and lower PL efficiency. Moreover, the $MoSe_2$ surface coverage in sample E is higher, contributing to an enhanced PL.

Given the enhanced PL behaviour of sample E, hereafter we will focus on the properties of this sample, starting with the elemental composition and stoichiometry studied by X-ray photoelectron spectroscopy (XPS). The Mo core level XPS spectrum is shown in Fig. 4a. The peaks at 232.1 and 229.0 eV binding energies (BE) are attributed to Mo $3d_{3/2}$ and $3d_{5/2}$ core levels, corresponding to Mo^{4+} in $MoSe_2$[26,27], giving a BE difference of 3.13 eV. The Se core level XPS spectrum of sample E is shown in Fig. 4b. The peak of Se around 55 eV can be divided into Se $3d_{5/2}$ and Se $3d_{3/2}$ with peak positions at 54.6 and 55.5 eV, respectively, and a BE difference of 0.9 eV, corresponding to Se^{2-} in $MoSe_2$[27]. The O 1 s spectrum (Fig. 4c) shows a single peak at 533.0 eV associated with the SiO_x layer from the oxidized substrate[28], thus confirming the absence of secondary phases, such as MoO_3 or MoO_2. Moreover, the ~1:2 Mo/Se ratio obtained from integrated peak areas, which were corrected by sensitivity factors, indicates that the $MoSe_2$ crystals have the desired stoichiometry.

The photovoltaic characteristics of the $Si/SiO_x/MoSe_2$ capacitors (sample E) were studied at room temperature and the results are plotted in Fig. 5. The black and red curves correspond to dark and light illumination conditions, respectively. J-V curves, under dark, of $Al/Si/SiO_x/MoSe_2/ITO$ capacitors exhibit diode behaviour, with a rectification ratio of 10, measured at ±2.0 V. The asymmetrical behaviour of the J-V curves, under dark, indicates that the diode behaviour of the samples is due to the p-i-n heterojunctions formed at $p\text{-}Si/SiO_x/MoSe_2$ interfaces. Consequently, a built-in electrical field (E_{bi}) is formed at the heterojunction. A turn-on voltage (V_{on}) of 1.0 V, where the current starts to increase quickly, can be obtained. This V_{on} is higher than the one observed in MoS_2/Si heterojunctions[22].

From the J-V curve under light conditions, a PV effect resulting in a finite short circuit current density (J_{sc}) and open circuit voltage (V_{oc}) is observed. For comparison, the PV response of samples C and D, together with that from sample E, is also given in Supplementary Fig. S1 online. The J_{sc} and the V_{oc} of samples C, D and E are 0.019, −0.76, −0.80 mA/cm^2 and −0.28, 1.30, 1.55 V, resulting in an efficiency of 0.002, 0.4 and 0.5%, respectively. The enhanced PV efficiency of sample E is associated with the different morphology including the shape, surface area covered, lateral size and thickness of the resultant $MoSe_2$ layers. Moreover, due to the high quality of our heterojunctions, the V_{oc} is significantly higher than the one observed in other p-i-n and p-n heterojuntions[22,29,30]. In

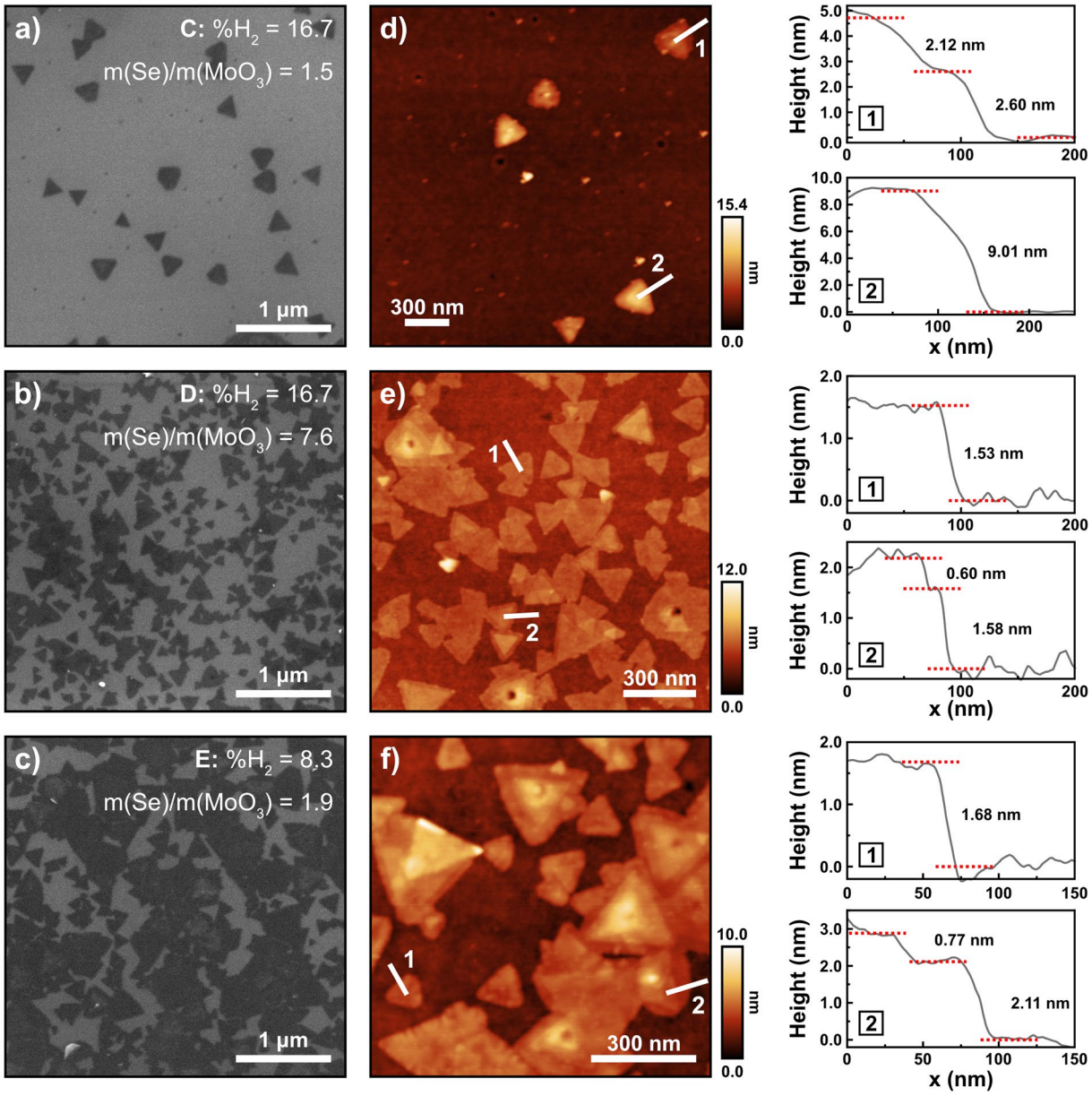

Figure 2. Scanning electron micrographs (**a**–**c**) of samples C, D and E, respectively, and their corresponding AFM images (**d**–**f**). The height profiles taken along lines 1 and 2 on the AFM images are shown on the right panel.

Sample	Average lateral size (nm)	Covered surface area (%)	Number of layers
A	154 ± 27	18 ± 1	Mono- and mono/bilayer
B	247 ± 100	31 ± 3	Mono- and multilayer
C	172 ± 44	Non uniform	Tri-/4-layer and multilayer
D	168 ± 59	49 ± 2	Bi- and mono/bilayer
E	278 ± 89	57 ± 7	Bi- and mono/trilayer

Table 2. Average lateral size of the triangle flakes and samples' surface area (in %) covered by triangles, as determined by SEM. The number of layers observed in the triangular structures is also presented.

fact, A. U. Rehman *et al*. showed that passivation enhances the built-in field by reduction of interface trap density at the surface[31]. However, while a SiO_x layer is essential for good passivation of the Si surface, an excessive SiO_x thickness (~160 nm in our samples) can decrease the effectiveness of the carrier tunneling due to scattering and trapping of the carriers in the SiO_x interlayer. Therefore, the J_{sc} is not so high leading to the degradation of the

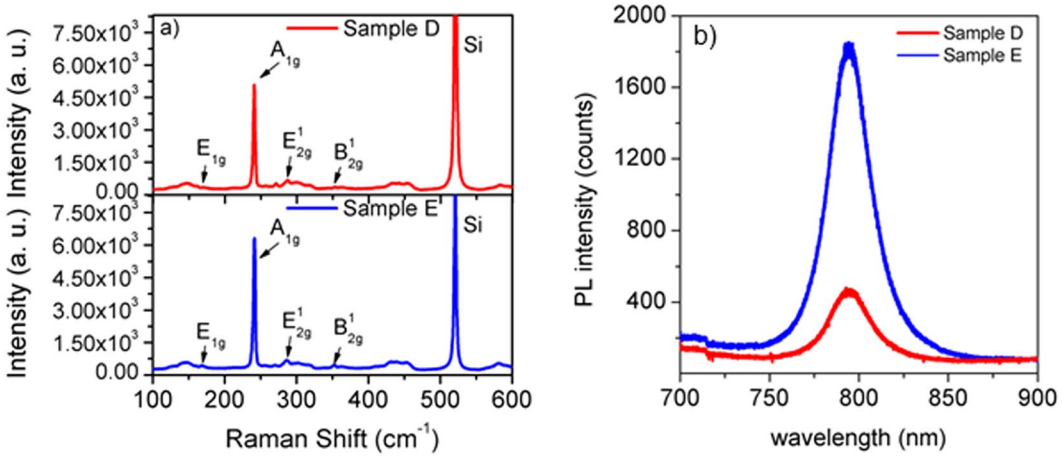

Figure 3. (**a**) Raman spectra of samples D and E, respectively. (**b**) Photoluminescence (PL) spectra of both samples.

PV efficiency. Nevertheless, the observed PV efficiency is similar to that observed in $MoSe_2/MoS_2$[32] and higher than the value found in $GaSe/MoSe_2$[33] heterojunctions based transistors; it is also higher than the one in $MoSe_2$ homojunctions based transistors, when measured at zero field[34].

Different strategies are being used to enhance the PV efficiency of MoS_2 based devices. For instance, the PV efficiency of MoS_2/Si p-n junctions was increased from 1.3%[22] up to 5.6% through the introduction of different passivation layers, such as SiO_2 and Al_2O_3, with also different thicknesses[31,35]. Moreover, it was shown that Pd chemical doping could increase the PV efficiency of MoS_2/Si hybrid solar cells by 375% to 2.4%[29].

Table 3 displays a comparison of the PV efficiency obtained in the present devices and the ones found in literature for different TMD based devices with different architectures. It is worth noting again that the present PV efficiency is at least similar to the best ones found in literature for $MoSe_2$ based devices. Furthermore, the outstanding V_{oc} value, which is significantly higher than the one observed in other p-i-n and p-n heterojunctions[22,29,30], is likely to encourage further research in this area, since the J_{sc} can be further increased through a number of strategies besides decreasing the thickness of the oxide layer, such as the coupling between $MoSe_2$ and plasmonic metal nanoparticles.

The photovoltaic mechanism in the Al/Si/SiO_x/$MoSe_2$/ITO capacitors can be understood as follows: under light illumination, the incident photons generate the electron–hole (e–h) pairs in the $MoSe_2$ film and Si, as shown in Fig. 6. The E_{bi} can effectively facilitate the separation and collection of photo-generated e–h pairs and the V_{OC} depends on the build-in potential across the interface. The processes of photo-excitation and carrier transport in the Si/SiO_x/$MoSe_2$ p-i-n junction are shown schematically in Fig. 6 showing the mechanisms responsible for photovoltaic action.

To separate the effects of enhanced photon absorption from carrier collection, photocurrent studies under different excitation photon energies were also performed and the corresponding external quantum efficiency (EQE) was determined. Figure 7 shows the EQE as a function of wavelength obtained from photocurrent measurements for sample E. From Fig. 7, it is possible to observe that the EQE increases with increasing photon energy in the visible and then abruptly decreases in the UV. As discussed by W.J. Yu *et al.*[39], when the EQE increases with the photon energy, one can assume that the enhanced absorbance is the primary factor responsible for the maximum EQE. For comparison, the EQE response of samples C and D together with the one from sample E is also given in Supplementary Fig. S2. The enhanced EQE of sample E can be related with the improved morphology including the shape, surface area covered, lateral size and thickness of the $MoSe_2$ flakes. Moreover, the observed EQE is at least one order of magnitude higher than that found in other $MoSe_2$ based devices[40], which clearly shows that the optimization of the $MoSe_2$ layers is crucial to significantly broaden the absorption spectrum, and to enhance the current conversion efficiency.

Conclusions

This work highlights the effect of two processing parameters, as the H_2 content and m(Se)/m(MoO_3) ratio, on the structural, microstructural and morphological characteristics of $MoSe_2$ layers. We observe that the introduction of H_2 in the gas flow is not per se sufficient to produce high-quality $MoSe_2$, and show that the ratio between the masses of precursors plays a key role in the formation of larger low dimensional $MoSe_2$ layers. The microstructural, optical and elemental characteristics revealed pure and stoichiometric $MoSe_2$ triangles. The photovoltaic characteristics of $MoSe_2/SiO_x$/Si heterojunctions were investigated. The PV response of the p-i-n heterojunction was evaluated and the PV efficiency is a result of the high built-in electric field developed at the heterojunction. The PV efficiency achieved is comparable to best results reported in the literature for $MoSe_2$ based devices. EQE measurements also confirmed that the enhanced absorbance in few-layers $MoSe_2$ is the primary factor for the maximum PV effect. Therefore, this work provides a guide to prepare few-layer $MoSe_2$ onto SiO_x/Si substrates for optoelectronic devices.

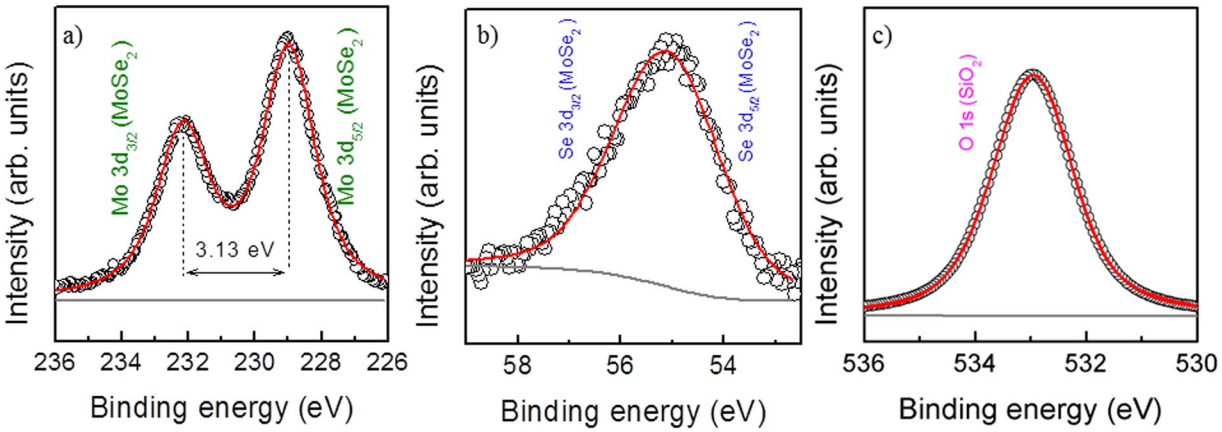

Figure 4. XPS spectra of (**a**) Mo, (**b**) Se and (**c**) O core levels for sample E.

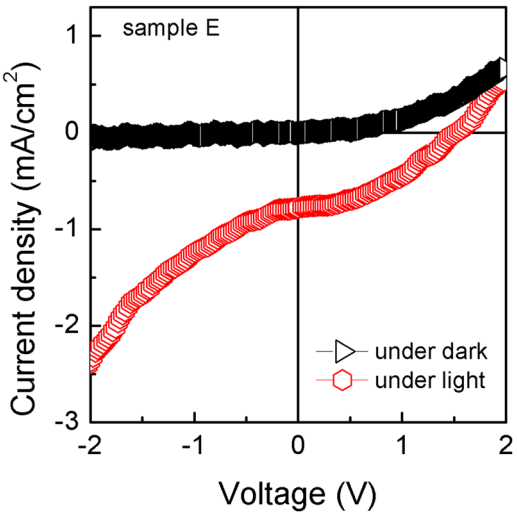

Figure 5. J-V curves under dark and light conditions for sample E.

TMDs	Architecture	PV efficiency (%)	Reference
$MoSe_2$	Vertical heterostructure	0.5	This work
$MoSe_2/MoS_2$	Transistor	≈0.5	[32]
$GaSe/MoSe_2$	Transistor	0.12	[33]
$MoSe_2$(thin)/ $MoSe_2$ (thick)	Transistor	≈0.1	[34]
MoS_2	Vertical heterostructure	1.3	[22]
MoS_2	Vertical heterostructure	4.5	[35]
MoS_2	Transistor	5.6	[31]
MoS_2	Vertical heterostructure	2.4	[29]
MoS_2	Vertical heterostructure	5.2	[36]
MoS_2	Vertical heterostructure	4.6	[37]
WSe_2 and WS_2	Transistor	0.7	[38]

Table 3. Comparison of the photovoltaic response obtained in this work with those presented in the literature for different TMD based devices.

Experimental details. Prior to the growth of $MoSe_2$ layers on SiO_x/Si substrates, the later were prepared in-house by the dry oxidation of p-doped (111) silicon wafer pieces, in a tube furnace at 930 °C and atmospheric pressure, using an oxygen flow rate of 100 sccm. The amorphous nature of the oxide layers was confirmed by X-ray diffraction (XRD) (not shown here).

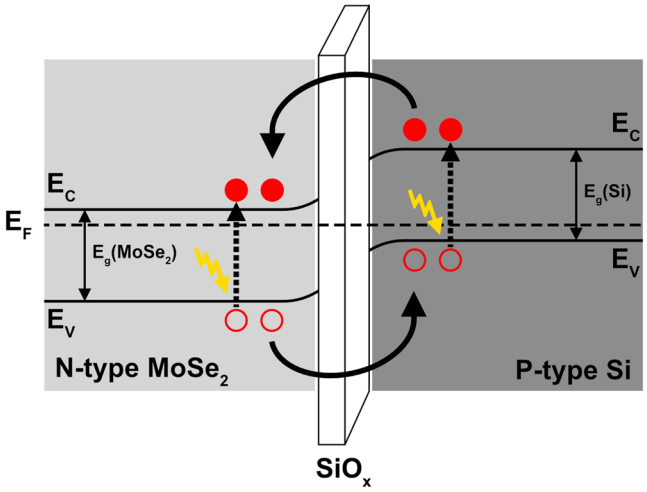

Figure 6. Energy band diagram of $MoSe_2/SiO_x/Si$ heterojunction. E_g is the energy band gap, E_f is Fermi-energy level, E_C is the bottom of conduction band and E_V is the top of valence band.

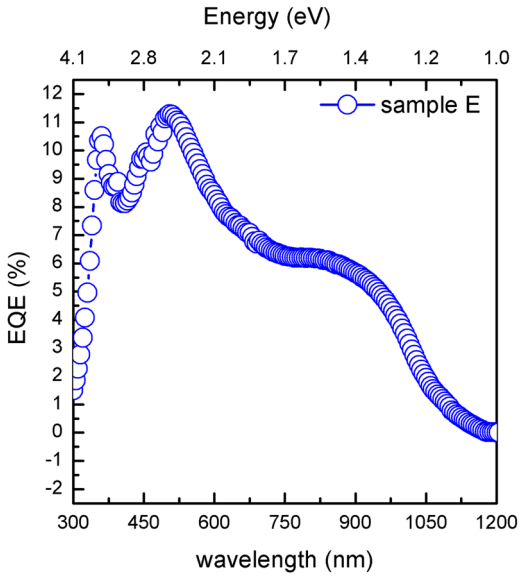

Figure 7. EQE as a function of wavelength for sample E.

The $MoSe_2$ nanolayers were grown in a CVD reactor composed of a 4 cm diameter quartz tube inside a 40 cm long tube furnace. MoO_3 powder (Neyco, 99.99% purity) and Se powder (Alfa Aesar, 99.999% purity) were loaded into quartz boats, at positions inside the reactor where their temperatures were 800 °C and 300 °C, respectively. The SiO_x/Si substrates were placed over quartz boats with the oxide layer facing down, 1 cm away from the MoO_3 boat at the downstream side, at a temperature of 790 °C.

The reactor was initially purged with Ar, at room temperature (RT), and then heated to 800 °C at a heating rate of 40 °C/min, keeping the Ar flux at 5 sccm. During the deposition, the Ar flux was increased and H_2 was added into the reactor, according to the deposition parameters shown in Table 3, for the five studied samples. The reactor was kept at the growth temperature for 15 min, after which it was naturally cooled to RT, using an Ar flow rate of 30 sccm.

The surface morphology of the samples was investigated by field emission scanning electron microscopy (FESEM, JEOL 7001 F) operating in secondary electrons imaging mode and atomic force microscopy (AFM, Multimode coupled to a Nanoscope IIIa, Digital Instruments, Bruker) in tapping mode. Additionally, the surface area covered by $MoSe_2$ triangle flakes and their average lateral size (Table 2) were obtained from the FESEM micrographs, by applying an intensity threshold to select the $MoSe_2$ layers and using the analyse particles function of the imageJ software. AFM was used to determine the number of layers of the triangles (Table 2), by measuring their height profiles, which are the average curves of five different measurements performed along equivalent trajectories on the AFM images.

Raman microprobe spectrometry and photoluminescence (PL) measurements were performed at RT to access the quality of the $MoSe_2$ flakes. For Raman spectroscopy, a LabRam HR800 Evolution (Horiba) system was used with a 532 nm excitation laser source and an 1800 grove/mm grating. The laser spot on the samples' surface was ~1 μm^2 and its power was ~10 mW. The excitation of the samples in the PL experiments was achieved by focusing the 514.5 nm line of an Ar^+ laser on the samples' surface, with a spot size less than 5 μm^2 and an excitation power less than 100 mW to avoid any heating and nonlinear optical effects. The scattered light was analysed by using a T64000 Horiba monochromator with a 100× objective, with single grating, and a liquid-nitrogen-cooled CCD camera, in the 700–900 nm spectral range and with a typical exposure time of 240 seconds.

Chemical composition and oxidation states of the films were evaluated by X-ray photoelectron spectroscopy (XPS). XPS was performed in UHV chamber equipped with a hemispherical energy analyzer Phoibos 150. In our experiments, we used the Mg source and the binding energy scale of all XPS spectra was calibrated according to the C 1 s reference (285.0 eV).

To perform the photovoltaic characterization, indium tin oxide (ITO) top electrodes with a diameter of 1 mm were deposited by ion-beam sputtering deposition (IBSD), as described in ref. [41], while Aluminium electrodes were attached to the Si wafer backside by electric spark. Current–voltage (I–V) characteristics, both in the dark and under light illumination, with a maximum power density of 100 $mWcm^{-2}$ (AM 1.5 G) were investigated. A computer controlled four-quadrant Source-Measure Unit was used to apply an external bias and measure the current. Additionally, the PV external quantum efficiency (EQE) was measured by using a Bentham PVE 300 system.

Received: 8 October 2019; Accepted: 7 January 2020;
Published online: 27 January 2020

References

1. Chhowalla, M. *et al*. The chemistry of two-dimensional layered transition metal dichalcogenide nanosheets. *Nat. Chem.* **5**, 263–275 (2013).
2. Shi, Y., Li, H. & Li, L.-J. Recent advances in controlled synthesis of two-dimensional transition metal dichalcogenides via vapour deposition techniques. *Chem. Soc. Rev.* **44**, 2744–2756 (2015).
3. Li, X. *et al*. Large-area synthesis of high-quality and uniform graphene films on copper foils. *Science* **324**, 1312–1314 (2009).
4. Kim, K. K. *et al*. Synthesis of monolayer hexagonal boron nitride on Cu foil using chemical vapor deposition. *Nano Lett.* **12**, 161–166 (2012).
5. Wang, S. *et al*. Shape evolution of monolayer MoS_2 crystals grown by chemical vapor deposition. *Mater.* **26**, 6371–6379 (2014).
6. Fu, Q. *et al*. Controllable synthesis of high quality monolayer WS_2 on a SiO_2/Si substrate by chemical vapor deposition. *RSC Adv.* **5**, 15795–15799 (2015).
7. Liu, B., Fathi, M., Chen, L., Abbas, A. & Zhou, C. Chemical vapor deposition growth of monolayer WSe_2 with tunable device characteristics and growth mechanism study. *ACS Nano.* **9**, 6119–6127 (2015).
8. Shaw, J. C. *et al*. Chemical vapor deposition growth of monolayer $MoSe_2$ nanosheets. *Nano Res.* **7**, 511–517 (2014).
9. Chen, T. *et al*. Controlled growth of atomically thin $MoSe_2$ films and nanoribbons by chemical vapor deposition. *2D Materials* **6**, 025002 (2019).
10. Lu, X. *et al*. Large-area synthesis of monolayer and few-layer $MoSe_2$ films on SiO_2 substrates. *Nano Lett.* **14**, 2419–2425 (2014).
11. Bachmatiuk, A. *et al*. Chemical vapor deposition of twisted bilayer and few-layer $MoSe_2$ over SiO_x substrates. *Nanotechnol.* **25**, 365603 (2014).
12. Lu, J. *et al*. Exfoliated nanosheet crystallite of cesium tungstate with 2D pyrochlore structure: synthesis, characterization, and photochromic properties. *ACS Nano* **11**, 1689–1695 (2017).
13. Xia, J. *et al*. CVD synthesis of large-area, highly crystalline $MoSe_2$ atomic layers on diverse substrates and application to photodetectors. *Nanoscale* **6**, 8949–8955 (2014).
14. Chang, Y. *et al*. Monolayer $MoSe_2$ grown by chemical vapor deposition for fast photodetection. *ACS Nano* **8**, 8582–8590 (2014).
15. Roy, T. *et al*. Field-effect transistors built from all two-dimensional material components. *ACS Nano* **8**, 6259–6264 (2014).
16. Benameur, M. M. *et al*. Visibility of dichalcogenide nanolayers. *Nanotechnol.* **22**, 125706 (2011).
17. Blake, P. *et al*. Making graphene visible. *Appl. Phys. Lett.* **91**, 063124 (2007).
18. Silva, J. P. B., Marques, C. A., Moreira, J. A. & Conde, O. Resistive switching in $MoSe_2$/$BaTiO_3$ hybrid structures. *J. Mater. Chem. C* **5**, 10353–10359 (2017).
19. Ding, G. *et al*. Metal-organic frameworks: 2D metal–organic framework nanosheets with time-dependent and multilevel memristive switching. *Adv. Funct. Mater.* **29**, 1806637 (***2019***).
20. Hsiao, K.-J., Liu, J.-D., Hsieha, H.-H. & Jiang, T.-S. Electrical impact of $MoSe_2$ on CIGS thin-film solar cells. *Phys. Chem. Chem. Phys.* **15**, 18174–18178 (2013).
21. Shim, G. W. *et al*. Large-area single-layer $MoSe_2$ and its van der Waals heterostructures. *ACS Nano* **8**, 6655–6662 (2014).
22. Hao, L. *et al*. Electrical and photovoltaic characteristics of MoS_2/Si p-n junctions. *J. Appl. Phys.* **117**, 114502 (2015).
23. Almeida Marques, C. Growth and characterization of low dimensional Mo selenide, MSc Thesis, University of Lisbon, http://hdl.handle.net/10451/25252 (2016).
24. Wang, H. *et al*. Revealing the microscopic CVD growth mechanism of $MoSe_2$ and the role of hydrogen gas during the growth procedure. *Nanotechnology* **29**(314001), 1–9 (2018).
25. Tongay, S. *et al*. Thermally driven crossover from indirect toward direct bandgap in 2D semiconductors: $MoSe_2$ versus MoS_2. *Nano Lett.* **12**, 5576–5580 (2012).
26. Xenogiannopoulou, E. *et al*. High-quality, large-area $MoSe_2$ and $MoSe_2$/Bi_2Se_3 heterostructures on AlN(0001)/Si(111) substrates by molecular beam epitaxy. *Nanoscale* **7**, 7896–7905 (2015).
27. Zhao, Y., Lee, H., Choi, W., Fei, W. & Lee, C. J. Large-area synthesis of monolayer $MoSe_2$ films on SiO_2/Si substrates by atmospheric pressure chemical vapor deposition. *RSC Adv.* **7**, 27969–27973 (2017).
28. Larina, T. V. *et al*. Influence of the surface layer of hydrated silicon on the stabilization of Co^{2+} cations in Zr–Si fiberglass materials according to XPS, UV-Vis DRS, and differential dissolution phase analysis. *RSC Adv.* **5**, 79898–79905 (2015).
29. Hao, L. Z. *et al*. Enhanced photovoltaic characteristics of MoS_2/Si hybrid solar cells by metal Pd chemical doping. *RSC Adv.* **6**, 1346–1350 (2016).
30. Hao, L. Z., Liu, Y. J., Han, Z. D., Xu, Z. J. & Zhu, J. Giant lateral photovoltaic effect in MoS_2/SiO_2/Si p-i-n junction. *J. Alloys and Comp.* **735**, 88–97 (2018).
31. Rehman, A. U. *et al*. n-MoS_2/p-Si solar cells with Al_2O_3 passivation for enhanced photogeneration. *ACS Appl. Mater. Interfaces* **8**, 29383–29390 (2016).
32. Yang, Y., Huo, N. & Li, J. Gate modulated and enhanced optoelectronic performance of $MoSe_2$ and CVD-grown MoS_2 heterojunctions. *RSC Adv.* **7**, 41052–41056 (2017).

33. Li, X. *et al*. Two-dimensional GaSe/$MoSe_2$ misfit bilayer heterojunctions by van der Waals epitaxy. *Sci. Adv.* **2**, e1501882 (2016).
34. Yang, Y., Huo, N. & Li, J. Gate tunable photovoltaic effect in a $MoSe_2$ homojunction enabled with different thicknesses. *J. Mater. Chem. C* **5**, 7051–7056 (2017).
35. Hao, L. H. *et al*. High-performance n-MoS_2/i-SiO_2/p-Si heterojunction solar cells. *Nanoscale* **7**, 8304–8308 (2015).
36. Tsai, M.-L. *et al*. Monolayer MoS_2 heterojunction solar cells. *ACS Nano* **88**, 8317–8322 (2014).
37. Xu, H. *et al*. Large area MoS_2/Si heterojunction-based solar cell through sol-gel method. *Mater. Lett.* **238**, 13–16 (2019).
38. Akama, T. *et al*. Schottky solar cell using few-layered transition metal dichalcogenides toward large-scale fabrication of semitransparent and flexible power generator. *Scientific Reports* **7**, 11967 (2017).
39. Yu, W. J. *et al*. Unusually efficient photocurrent extraction in monolayer van der Waals heterostructure by tunnelling through discretized barriers. *Nat. Commun.* **7**, 13278 (2016).
40. Flöry, N. *et al*. A WSe_2/$MoSe_2$ heterostructure photovoltaic device. *Appl. Phys. Lett.* **107**, 123106 (2015).
41. Silva, J. P. B. *et al*. Enhanced resistive switching characteristics in Pt/$BaTiO_3$/ITO structures through insertion of HfO_2:Al_2O_3 (HAO) dielectric thin layer. *Scientific Reports* **7**, 46350 (2017).

Acknowledgements

This work was supported by the Portuguese Foundation for Science and Technology (FCT) in the framework of the Strategic Funding Contracts UID/CTM/04540/2019 and UID/FIS/04650/2019. Part of this work was supported by the COST Action MP1406 "Multiscale in modeling and validation for solar photovoltaics (MultiscaleSolar)". The authors acknowledge the CERIC-ERIC Consortium for access to experimental facilities and financial support under proposal 20182042.

Author contributions

J.P.B.S., C.A.M. and O.C. conducted sample synthesis, characterization, and data analysis. A.S.V. and L.F.S. assisted with AFM and Raman studies, respectively, and associated data analysis. K.V. and V.M. performed the XPS measurements and analysis. K.G., E.P. and J.P.C. performed the PL and PV measurements and analyses. O.C. conceived and designed the experiments and together with J.P.B.S. wrote the manuscript. All authors commented on the manuscript.

Competing interests

The authors declare no competing interests.

Additional information

Supplementary information is available for this paper at https://doi.org/10.1038/s41598-020-58164-7.

Correspondence and requests for materials should be addressed to J.P.B.S. or O.C.

Reprints and permissions information is available at www.nature.com/reprints.

Publisher's note Springer Nature remains neutral with regard to jurisdictional claims in published maps and institutional affiliations.